The EMBO Journal (2011) 30, 1719–1729 | © 2011 European Molecular Biology Organization | All Rights Reserved 0261-4189/11
www.embojournal.org

THE EMBO JOURNAL

Lateral density of receptor arrays in the membrane plane influences sensitivity of the *E. coli* chemotaxis response

Cezar M Khursigara[1,5,6], Ganhui Lan[2,6], Silke Neumann[3], Xiongwu Wu[4], Suchie Ravindran[1], Mario J Borgnia[1], Victor Sourjik[3], Jacqueline Milne[1], Yuhai Tu[2,*] and Sriram Subramaniam[1,*]

[1]Laboratory of Cell Biology, Center for Cancer Research, National Cancer Institute, National Institutes of Health, Bethesda, MD, USA, [2]IBM T. J. Watson Research Center, Yorktown Heights, NY, USA, [3]Zentrum für Molekulare Biologie der Universität Heidelberg, DKFZ-ZMBH Alliance, Heidelberg, Germany and [4]Laboratory of Biophysical Chemistry, National Heart, Lung, and Blood Institute, National Institutes of Health, Bethesda, MD, USA

In chemotactic bacteria, transmembrane chemoreceptors, CheA and CheW form the core signalling complex of the chemotaxis sensory apparatus. These complexes are organized in extended arrays in the cytoplasmic membrane that allow bacteria to respond to changes in concentration of extracellular ligands via a cooperative, allosteric response that leads to substantial amplification of the signal induced by ligand binding. Here, we have combined cryo-electron tomographic studies of the 3D spatial architecture of chemoreceptor arrays in intact *E. coli* cells with computational modelling to develop a predictive model for the cooperativity and sensitivity of the chemotaxis response. The predictions were tested experimentally using fluorescence resonance energy transfer (FRET) microscopy. Our results demonstrate that changes in lateral packing densities of the partially ordered, spatially extended chemoreceptor arrays can modulate the bacterial chemotaxis response, and that information about the molecular organization of the arrays derived by cryo-electron tomography of intact cells can be translated into testable, predictive computational models of the chemotaxis response.

The EMBO Journal (2011) **30,** 1719–1729. doi:10.1038/emboj.2011.77; Published online 25 March 2011
Subject Categories: signal transduction
Keywords: chemotaxis; cryo-electron tomography; receptors; signal transduction

*Corresponding authors. S Subramaniam, Laboratory of Cell Biology, Center for Cancer Research, National Cancer Institute, National Institutes of Health, Bldg. 50, Rm. 4306, Bethesda, MD 20892, USA. Tel.: +1 301 594 2062; Fax: +1 301 480 3834; E-mail: ss1@nih.gov or Y Tu, IBM T. J. Watson Research Center, Yorktown Heights, NY, USA. Tel.: +1 914 945 2762; Fax: +1 914 945 4506; E-mail: yuhai@us.ibm.com
[5]Present address: Department of Molecular and Cellular Biology, University of Guelph, Guelph, ON, Canada N1G 2W1
[6]These authors contributed equally to this work

Received: 20 October 2010; accepted: 23 February 2011; published online: 25 March 2011

Introduction

Signal transduction in bacterial chemotaxis relies on a chemosensory signalling apparatus that receives and transmits chemical signals from the environment to the cell to control the motility system that produces cell movement. Transmembrane chemoreceptors, also known as methyl-accepting chemotaxis proteins (MCPs), coordinate cell movement by regulating the histidine autokinase CheA, which controls the direction of the flagella rotation by modulating the intracellular levels of the response regulator phospho-CheY (CheY-P).

Chemoreceptors are composed of four functionally distinct regions: the ligand-binding periplasmic domain, the transmembrane domain, the 'HAMP' signalling domain, and a long cytoplasmic domain (reviewed in Hazelbauer *et al* (2008)). Chemoreceptors and CheA form a ternary complex with the adaptor protein CheW (Gegner *et al*, 1992), and have a crucial role in signal processing (Wadhams and Armitage, 2004; Hazelbauer *et al*, 2008; Sourjik and Armitage, 2010). These core ternary-signalling complexes cluster primarily (Maddock and Shapiro, 1993; Sourjik and Berg, 2000), but not exclusively (Thiem *et al*, 2007) to the poles of *E. coli* cells.

Cryo-electron tomographic studies have allowed visualization of the extended chemoreceptor arrays at the polar region of various bacterial species (Zhang *et al*, 2007; Borgnia *et al*, 2008; Briegel *et al*, 2008, 2009; Khursigara *et al*, 2008a). These studies demonstrate that the signalling complexes are arranged in distinct, dense clusters, with approximately hexagonally packed arrays of trimers of chemoreceptor dimers in the plane of the membrane (Briegel *et al*, 2008, 2009; Khursigara *et al*, 2008a). This arrangement is only partially ordered, suggesting that hexagonal packing may arise largely from the high local density of receptors in the membrane plane.

Structural studies have also shown that chemoreceptor trimers-of-dimers exist in an equilibrium between two conformational states that appear to correspond to compact and expanded conformations of the HAMP signalling domains (Khursigara *et al*, 2008b). Binding of chemoattractants favours a shift in the equilibrium towards the expanded state, whereas methylation of receptors favours the compact state. Starting with this two-state conformational equilibrium, the dynamic features of the chemotaxis signalling pathway are hypothesized to emerge through multiple levels of protein interactions, ranging from the formation of chemoreceptor trimer-of-dimers to the association of a ternary receptor signalling complex that includes CheA and CheW, and culminating in the formation of ordered arrangements containing thousands of ternary complexes (Kentner and Sourjik, 2006; Hazelbauer *et al*, 2008). Attractant binding to chemoreceptors inhibits CheA-kinase activity to reduce the concentration of the soluble mediator CheY-P. Methylation of the chemoreceptors counters the ligand-induced inhibition of kinase activity. The balance between ligand occupancy and

methylation maintains the ability of the system to respond to a wide range of ligand concentrations (Hazelbauer *et al*, 2008).

The ability of the chemoreceptor assembly to amplify the signals derived from ligand binding, and the allosteric nature of the chemotaxis response, represent two unique features of the signalling pathway of bacterial chemotaxis. Thus, inactivation of the CheA kinase in the cytoplasm can be ~100 times higher than would be predicted from the change in ligand occupancy of the periplasmic domain of the receptor (Segall *et al*, 1986). The allosteric response is believed to arise from the cooperative interactions of chemoreceptors within the array, with the slope of the dose–response curve measuring the sensitivity of the overall response (Sourjik and Berg, 2002a). Understanding the mechanisms of the cooperativity and signal amplification are therefore questions of fundamental interest. Here, we address this problem by combining: (i) cryo-electron tomography to explore key physical elements important in the organization of the chemoreceptor array, (ii) computational studies that use the tomographic information to generate predictive models for the signalling response, and (iii) FRET experiments to test these theoretical predictions experimentally *in vivo* under the same conditions as those used for the tomographic experiments.

Results

Visualization of chemoreceptor arrays in intact cells

To define quantitative aspects of chemoreceptor array assemblies, we used cryo-electron tomography to image intact, plunge-frozen *E. coli* cells. Partially ordered, spatially extended chemoreceptor arrays can be visualized in whole bacterial cells (Figure 1A). The approximately local hexagonal arrangement of chemoreceptors, with a lattice spacing of ~11 nm is evident in a 'face-on' orientation image (Figure 1A, top inset), in which the long axis of the chemoreceptors is parallel to the incident electron beam. The presence of local order is confirmed upon inspection of the computed optical diffraction pattern of this region of the image (Figure 1A, bottom inset). The cellular chemoreceptor assemblies can also be visualized in 'edge-on' views as illustrated in Figure 1B, in which the long axis of the receptors is orthogonal to the incident electron beam (Figure 1B and C). The vast majority of cellular tomograms contain chemoreceptor arrays imaged in this edge-on orientation. By rotating the volumes of 3D stacks of images collected with the receptors in this orientation by 90°, views of the lateral distribution of the receptors in the face-on orientation can be computed, and averaged with hexagonal symmetry (Figure 1B, inset). This computed packing arrangement also has a lattice spacing of ~11 nm, that is the same as that obtained from the face-on arrays; the face-on and edge-on

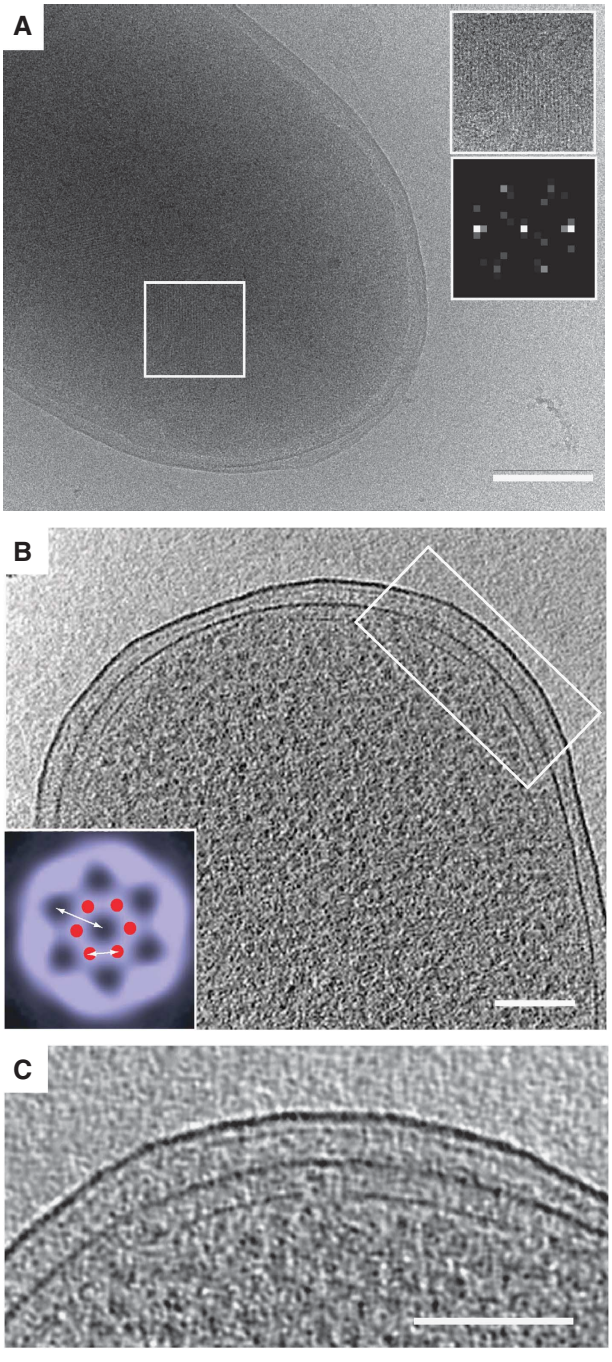

Figure 1 Cryo-electron microscopy and tomography of chemoreceptor arrays from frozen-hydrated *E. coli* cells. (**A**) A projection image recorded from a plunge-frozen *E. coli* cell using low-dose cryo-electron microscopy. The image shows patches of chemoreceptor arrays in the face-on orientation within the cytoplasmic membrane (white box). The bottom inset is an expanded view of the quasi-hexagonal order exhibited by the packing of chemosensory molecules in the membrane area, and the top inset is an optical diffraction pattern computed from the same region. (**B**) A tomographic slice (~5 nm thick) taken from a three-dimensional volume of the polar regions of an intact *E. coli* cell cultured in TB medium. Continuous and intact outer and cytoplasmic membranes are observed. The chemoreceptor arrays (white box) are evident and characterized by the presence of chemoreceptor striations sandwiched between the cytoplasmic membrane and the line of density representing the signalling scaffolds. The inset demonstrates the hexagonal packing arrangement of chemosensory proteins obtained by volumetric averaging from multiple edge-on arrays. The purple areas represent averaged densities with the red circles representing the locations of signalling molecules within the hexagonal unit. The small white arrow denotes the receptor-to-receptor distance of ~7 nm, while the larger white arrow denotes the ~11 nm lattice spacing. (**C**) An expanded view of the chemoreceptor array presented in panel B. Scale bars = 100 nm.

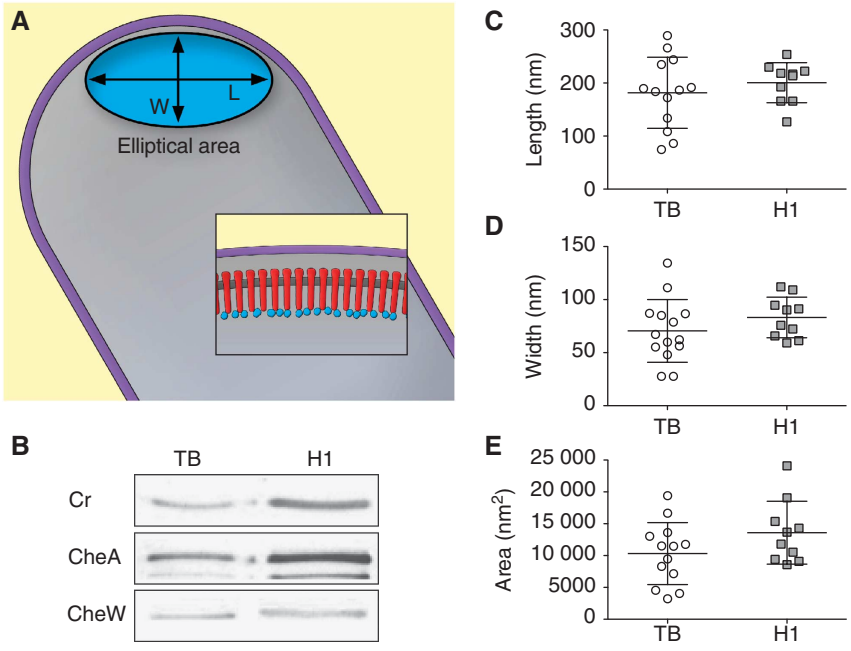

Figure 2 Effect of varying nutrient conditions on the size of *E. coli* chemoreceptor arrays. (**A**) Schematic illustration of the location, dimensions, and organization (inset) of chemoreceptor arrays in intact cells. (**B**) The levels of chemoreceptors (Cr), CheA, and CheW in *E. coli* cells that were cultured in either TB (○) or H1 (▩) media, assessed by western blotting using antibodies against the respective proteins as previously described (Zhang *et al*, 2007). (**C–E**) Chemoreceptor arrays were segmented from tomographic volumes of the polar regions of frozen-hydrated *E. coli* cells cultured in either TB (○) or H1 (▩) media (same nutrient conditions as analysed by western blotting) and the dimensions of the arrays were measured as described in (**A**). The plots display the mean lengths (**C**), widths (**D**), and areas (**E**) derived from the tomographic volumes (as described in (**A**)) and the variations between the two growth conditions.

views, therefore, provide equivalent information on the average packing arrangement of the chemoreceptors.

In addition to determining the average packing arrangement, the tomographic volumes can also be analysed to extract values for the dimensions of the chemoreceptor arrays in each cell to provide a measure of the extent of variation of these parameters across the cell population and across different growth conditions (Figure 2). Previous studies indicate that the levels of chemoreceptor, CheA and CheW protein expression change dependent on the nutrient content of the growth media (Li and Hazelbauer, 2004; Zhang *et al*, 2007). To determine whether these changes in expression level might correlate with changes in dimensions of the chemoreceptor array, we directly visualized their dimensions by cryo-electron tomography. Compared with cells grown in rich medium (tryptone broth, henceforth denoted as TB), cells grown in minimal medium (H1) show higher levels of chemoreceptors and CheA/CheW expression as assessed by western blot analysis (Figure 2B). Measurements of the lengths (Figure 2C), widths (Figure 2D), and estimated areas (Figure 2E) of the chemoreceptor array show that while the dimensions of the arrays can vary considerably even within a single population of cells, the average size is similar for cells grown in TB or H1. Therefore, the significant (>2-fold) increase in chemoreceptor and CheA expression levels observed for cells grown in H1 is not directly translated into an increased size of the chemoreceptor array. Moreover, the increased expression in H1 is not expected to affect the stoichiometry of the sensory complexes, because the levels of receptors, CheA and CheW increase proportionally (Figure 2B).

Distribution of signalling complexes within chemoreceptor arrays

To further investigate the structural parameters that may be most relevant for influencing changes in sensitivity of the chemotaxis response under different growth conditions, we analysed the distribution of signalling complexes *within* chemoreceptor arrays. For this purpose, we started with whole cell tomograms, and created distribution maps of the locations of the signalling complexes in each cell, which provide information about the local packing density of the chemoreceptor/CheA/CheW complexes in the plane of the membrane (Figure 3A and B). Previous cryo-immunolabelling experiments have established the presence and relative spatial distribution of chemoreceptors, CheA and CheW within the array (Zhang *et al*, 2007). These distribution maps were then used to derive plots to describe the organization of signalling complexes within a given chemoreceptor array, represented as the variation in distribution patterns relative to the distance between signalling complexes (Figure 3C). The position of first peak (r_{nn}) in this distance distribution plot provides a quantitative measure of the relative proximity of signalling complexes to their neighbours within the arrays. The peaks in the distribution plots can be understood as a direct measure of the constraints that govern the close packing of the complexes, demonstrating that even in the absence of perfect order, a clear periodicity in packing can be observed, corresponding to the approximate hexagonal packing of the chemoreceptor arrays. In addition to these distribution plots, it is possible to create diagrams that represent the 'connectedness' of the array by using a cutoff distance for nearest neighbours (set here as $1.5r_{nn}$, see

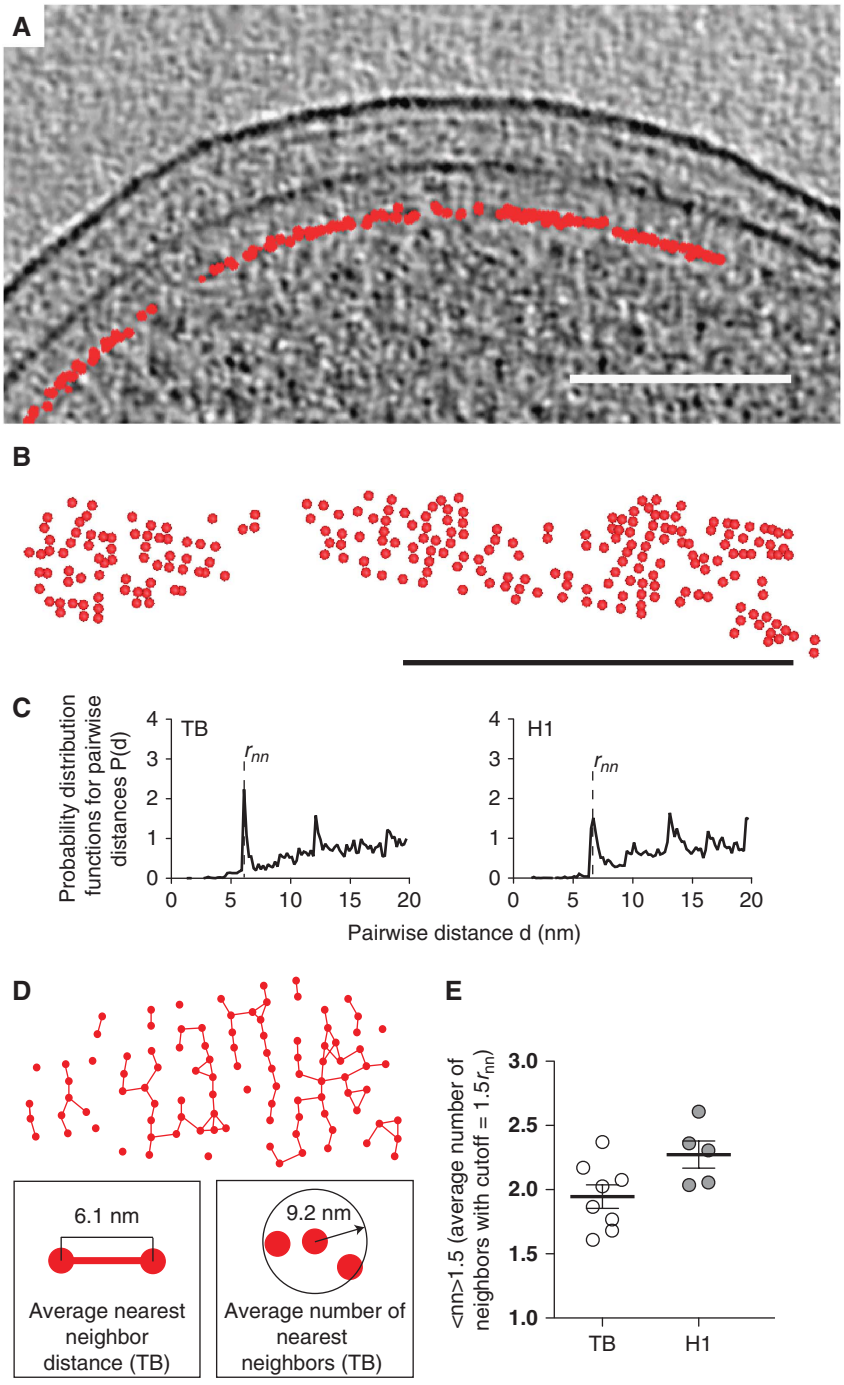

Figure 3 Spatial distribution of signalling complexes within chemoreceptor arrays. (**A**) A tomographic slice (5 nm thick), same as that displayed in Figure 1C, but with the densities corresponding the chemoreceptor–CheA/W interface segmented in red. Scale bar is 100 nm. (**B**) The edge-on segmented array from (**A**) was rotated by ~90° to obtain the in-plane distribution of chemosensory molecules comprising the array. (**C**) The probability density functions $P(d)$ for pairwise distance r between centres of chemosensory complex densities within an array for *E. coli* cells cultured in TB and H1 media. The position (r_{nn} as shown in the figure) of the first peak in $P(d)$ can be used to define the average nearest neighbour distance within an array for each bacterium. (**D**) A representative segmented chemoreceptor array from an *E. coli* cell cultured in TB demonstrating the nearest neighbour associations using procedures described in more detail in Materials and methods. The bottom left inset describes the average 6.1 nm spacing between two chemosensory complexes, while the bottom right inset describes the average number of chemosensory complexes located within the determined cutoff radius. (**E**) Plot of number of nearest neighbours, with the number for a given spot defined as those neighbours within a cutoff distance that can be chosen between the first and the second peak positions of $P(d)$. Each symbol represents a distinct cell, while the solid lines represent the average for each growth condition. Chemoreceptor arrays in *E. coli* cultured in H1 demonstrate increased connectivity in its chemoreceptor arrays compared with *E. coli* cultured in TB.

Materials and methods for more details), where nearest neighbours in an array are linked by a bond (Figure 3D). Larger values for the number of nearest neighbours indicate a tighter array structure, with a maximum possible value of six nearest neighbours for a perfectly packed hexagonal arrangement. Analysis of the averaged lateral packing reveals

that for *E. coli* cells cultured in H1, the average number of nearest neighbours is ~2.3, while for cells cultured in TB, the average number of nearest neighbours shows a broad distribution with an average of 1.9 nearest neighbours (Figure 3E). The distance distribution plots in Figure 3C and the packing density values in Figure 3E provide distinct and complementary information for the arrangement of receptors in cells grown in H1 and TB. On average, each signalling complex in the H1 receptor array has more nearest neighbours than in the case of the TB array, but these neighbours are also a little further apart than they are in the case of the TB receptor array. The small increase in mean distance between complexes in the H1-grown cells may in fact be a direct reflection of the higher occupancy of CheA in the lattice and its expansion to accommodate the higher lateral protein density at the base of the cytoplasmic membrane.

Ising model for disordered E. coli chemoreceptor signalling arrays

The variation in close packing of sensory molecules in *E. coli* cells cultured in TB versus H1 media suggests that the local packing density may be an important parameter for regulating the sensitivity of the chemotaxis response. If the functional difference between TB- and H1-grown cells derives from changes in the distribution of sensory molecules, it should then be possible to develop computational models that capture this difference and allow the formulation of predictive, testable models for the sensitivity of the chemotaxis response. To this end, we developed a model for chemoreceptor cooperativity within the chemoreceptor array using an Ising-type model (Bray *et al*, 1998; Duke and Bray, 1999; Mello and Tu, 2003), in which individual functional units in an array interact between nearest neighbours. The individual functional unit in the array, characterized by its ligand-binding affinity and kinase-stimulating activity, is kept constant for cells in different media. The chemoreceptor array structure, determined by cryo-electron tomography, was used directly to model interactions between neighbouring functional units, and the computational model was used to predict the cellular response to a given stimulus from its measured chemoreceptor array structure.

Using the Ising model, we computed the dose–response function for each of the cells whose chemoreceptor array structure was determined by cryo-electron tomography (Figure 4). The response is the calculated activity of the adapted sensory array. The sensory systems were first allowed to adapt to a background ligand concentration, $[L]_0 = 10K_I$, where K_I is the ligand dissociation constant for the inactive state of the receptor. The activity response was then calculated over four orders of magnitude in ligand concentration, from $10^{-1}K_I$ (i.e., for a decrease in the ligand concentration) to 10^3K_I (i.e., for an increase in the ligand concentration), while keeping the receptor methylation level unchanged. An important result from our calculations is that although the chemoreceptor arrays are not a highly ordered crystalline structure, they are still capable of producing a sharp response to changes in ligand concentration, hence ensuring high sensitivity (Figure 4, compare black dashed line with blue and red lines). The computed response curves also show that *E. coli* cells grown in H1 are more sensitive than cells cultured in TB, as measured by the Hill coefficient

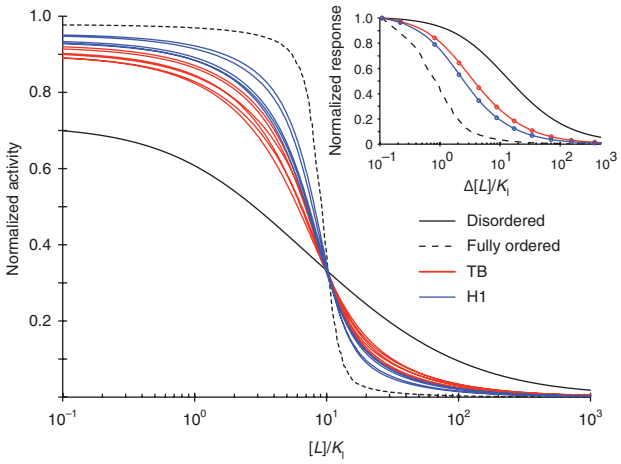

Figure 4 Computed dose–response curves. Results from simulation of chemoreceptor assemblies responding to a change in ligand concentration based on experimentally observed array distributions. In the main plot, red lines are response curves calculated for *E. coli* cells cultured in TB, blue lines are calculated for *E. coli* cells cultured in H1, and the black line is the control situation for chemoreceptors that are completely disordered. The ligand environment that chemoreceptor arrays are pre-adapted to is $[L]_0 = 10K_I$, where K_I is the ligand dissociation constant for the inactive state of the receptor. The plots can be used to derive 'sensitivity' of the response, measured as the slope of the response curve. The inset curves are the normalized response of above three categories when ligand concentration is increased. Tighter packing of chemoreceptors results in a more 'sensitive' response, and on average, cells cultured in H1 (blue lines) display ~30% higher sensitivity than those cultured in TB (red lines).

of the dose–response curve (Figure 4, blue lines are steeper than red lines). In the inset of Figure 4, we re-plot the portion of the activity curve that corresponds to the post-adaptation response to an increase in the ligand concentration (bottom right side of Figure 4, from $x = 10^1$ $[L]/K_I$ and $y = \sim 0.33$). The main difference between the main plot and the inset is that the *x*-axis in the inset represents the 'additional' ligand concentration (i.e., the increase relative to the concentration to which the system has already adapted), and the *y*-axis response represents the extent of the change in the chemotaxis response when the concentration of attractant is increased. On average, growth in H1 results in an ~30% increase in sensitivity compared with growth in TB (Figure 4, *inset*). Our modelling results clearly indicate that *E. coli* cells become more sensitive to nutrient stimuli under less favourable growth conditions.

Experimental test of the computational model

The computational model described above predicts that in *E. coli* cells, the sensitivity of the chemotaxis response (Hill coefficient of the response) can change by as much as a factor of ~2 with differing packing arrangements of the chemoreceptor array, which, in turn, are influenced by changes in the nutrient content of the culturing media. To test this hypothesis, we employed fluorescence resonance energy transfer (FRET) (Sourjik and Berg, 2002a, 2004) to monitor the activity of the receptor-coupled CheA-kinase activity in adaptation-deficient *E. coli* cells that express only one major receptor, Tar, cultured in TB and H1 media. The FRET assay relies on phosphorylation-dependent interaction of the chemotaxis response regulator CheY fused to yellow

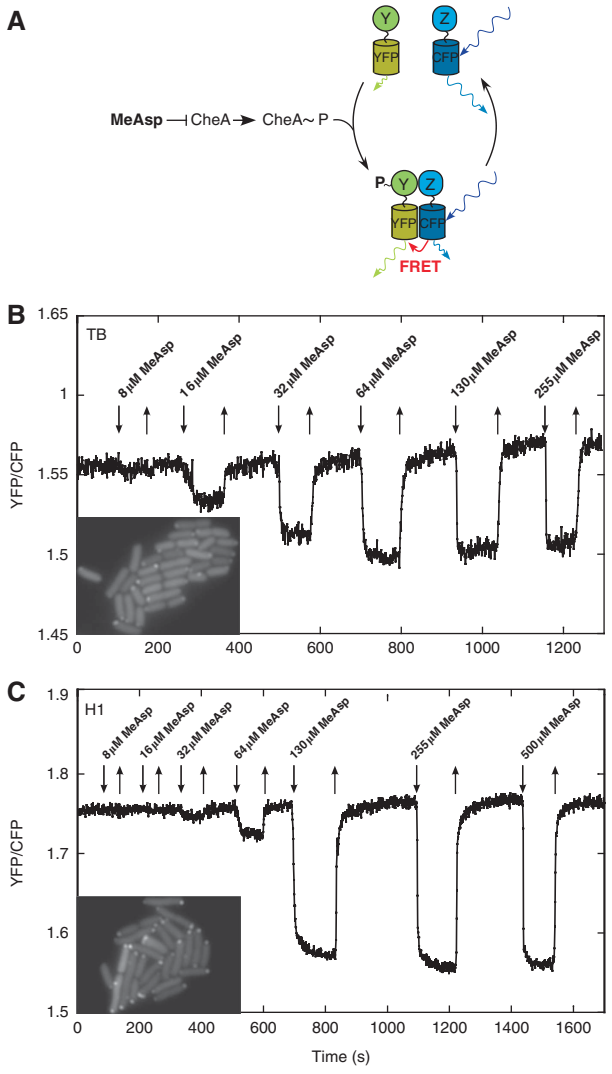

Figure 5 Intracellular FRET measurement of chemosensory complex response. (**A**) Schematic illustration of the FRET-based assay of the sensory complex activity. FRET reflects the intracellular amount of the complex between phosphorylated response regulator CheY and its phosphatase CheZ, thus providing a direct output of CheA activity. Addition of attractant (MeAsp) inhibits CheA activity in a dose-dependent manner as shown in dose–response measurements (**B**) and (**C**) for a *tsr cheR cheB* strain (VS151) grown in TB (**B**) or H1 (**C**). Insets show chemoreceptor arrays marked by YFP–$CheA_S$ in the same strain grown under identical conditions.

fluorescent fusion protein (CheY–YFP), with its phosphatase CheZ fused to cyan fluorescent fusion protein (CheZ–CFP) (Figure 5A). Under our experimental conditions, CheY is phosphorylated by CheA at the same rate at which CheY-P is dephosphorylated by CheZ, so kinase activity can be inferred from the concentration of the CheZ–CheY-P enzyme–substrate complex. The latter can be calculated from the extent of energy transfer from CFP to YFP, monitored as changes in the ratio of YFP/CFP fluorescence (Figure 5B and C) (Sourjik *et al*, 2007). The effects of adaptation are not a factor in these experiments, as CheR and CheB are not expressed in these cells. Upon the addition of the attractant α-methyl-aspartate (MeAsp), CheA activity is reduced in a dose-dependent manner indicated by the dips in the plots (Figure 5B and C).

The experimental findings demonstrate unequivocally that cells grown in H1 responded with a much steeper dose dependence, indicating their higher sensitivity to small changes in ligand concentration as predicted by theoretical modelling (Figure 4). The larger response amplitude reflects the higher expression levels of chemotaxis proteins in cells grown in H1 (Figure 2B), in excellent agreement with cryo-electron tomographic studies of wild-type *E. coli* cells that show progressive increases in the levels of chemotaxis proteins with a decrease in 'richness' of the growth media (Zhang *et al*, 2007) (Figure 2B) and with the increased fluorescence intensity of the chemoreceptor array in H1-grown cells as compared with TB-grown cells (insets of Figure 5B and C).

In Figure 6, we present a direct comparison of the experimentally derived plot of the responses to changes in ligand concentration for TB- and H1-grown cells with the theoretical predictions from the Ising model. The experimentally observed responses in Figure 5B and C provide data points that determine the slopes of the response curves, confirming that the Hill coefficient is higher for cells grown in H1 as compared with TB. Notably, because the adaptation-deficient cells used here have high levels of receptor activity, interactions between receptors further tend to stabilize them in the active state. It is thus the Hill coefficient and not the threshold ligand concentration that reflects the interaction strength between receptors under our experimental conditions. The observed differences between the dose–response curves for TB- and H1-grown cells could indeed be well reproduced assuming different density of receptor packing. The computed responses are shown as predictions for individual cells, representing an averaged response for each growth condition. For comparison, the predicted response for a disordered arrangement of the signalling complexes is also shown. Despite some deviations in the steepness of the response, the predicted curves show remarkably good agreement with the experimental data, and capture the overall trends of the response in both TB- and H1-grown cells. This agreement between theoretical and experimental results provides experimental validation for our hypothesis that changes in lateral density of chemoreceptor packing represents a central aspect of the cellular response to changes in growth media. The results also establish that perfect hexagonal packing is not a prerequisite for producing the characteristic steep cellular response; partially ordered, close-packed chemoreceptor arrays are capable of producing a cooperative response with a high Hill coefficient upon changes in ligand concentrations.

One important remaining and testable question is whether the computational model also correctly captures the experimental finding (Figures 2 and 3) that the differences between TB- and H1-grown cells arise primarily from differences in packing density and not in the overall size or stoichiometry of the chemoreceptor arrays. To evaluate this, we started with a distribution of chemoreceptor complexes as determined by cryo-electron tomography, and computed the dose–response curves before and after reducing the size of the array to either 70 or 40% of its initial size (Figure 7A and B). In a separate set of experiments, we started with two synthetic lattices of the same size, packed with chemoreceptor complexes at packing densities corresponding to those observed for cells grown under TB or H1 media, and computed the

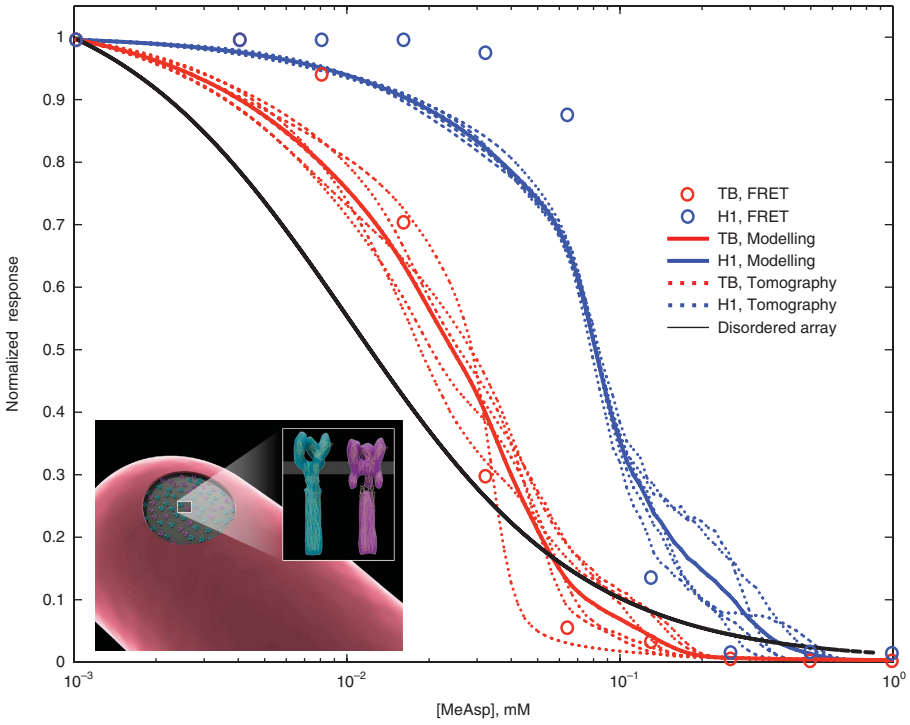

Figure 6 Comparison of nearest neighbour modelling with functional FRET analysis. A comparison of the response curves predicted from the Ising model (red and blue lines for *E. coli* cells cultured in TB and H1, respectively) with the response curves measured from the functional FRET analyses (red and blue open circles for *E. coli* cells cultured in TB and H1, respectively). The theoretical predictions were carried out using the same conditions used in the model in Figure 4, but without adaptation (see Materials and methods). The plot demonstrates good agreement between the model results and the experimental data over the entire MeAsp concentration range for both cells cultured in rich and minimal media. The black line represents a condition where chemosensory molecules are completely disordered and the response shows no cooperativity. The inset shows a schematic representation of the receptor array in the cytoplasmic membrane, with expanded views of the experimentally determined density maps for the 'open' and 'closed' conformations of the receptors in the array.

dose–response curves as above (Figure 7C and E). Comparison of the predicted response curves shows that small changes in size of receptor array (100 versus 70%) do not lead to significant changes in the dose–response curve, but as the size is reduced drastically (100 versus 40%), the response curves shift towards the response predicted for a disordered array in which none of the complexes have any nearest neighbours as defined in the plots shown in Figure 3D (Figure 7B). However, maintaining the size, but increasing the packing density of the synthetic lattice results in a large increase in cooperativity (Figure 7E), as observed in the FRET experiments (plot in Figure 6). These *in silico* experiments therefore verify that the computational model reflects the principal structural and functional parameters determined in the tomographic and FRET experiments.

Discussion

First proposed by Dennis Bray (Bray *et al*, 1998), the idea of signal amplification through receptor clustering has attracted a great deal of attention and has gained substantial support from both *in vitro* (Li and Weis, 2000; Bornhorst and Falke, 2003) and *in vivo* (Sourjik and Berg, 2002a, b, 2004) measurements. However, the molecular mechanism and the structural basis for the heightened sensitivity remain unclear. Do the receptors form an extended ordered lattice (Shimizu *et al*, 2003; Briegel *et al*, 2009) of tightly packed signalling molecules in the plane of the membrane? Or do they form tightly coupled 'all-or-none' complexes with a finite number of receptors, as described by the Monod–Wyman–Chandeux (MWC) allosteric model (Sourjik and Berg, 2004; Mello and Tu, 2005; Keymer *et al*, 2006; Hansen *et al*, 2010)? Our study shows that the real arrangement of chemoreceptors in bacteria is best described by something that is intermediate to these extreme scenarios. There is no biochemical or structural evidence that the chemoreceptor signalling complexes form well-defined allosteric complexes with known stoichiometry, nor that they are required to form a regularly ordered lattice to carry out chemotaxis function. Our experiments show instead that the signalling complexes form spatially extended networks with varying degrees of connectedness. However, this finding does not rule out the high overall stability of the underlying signalling complexes (Schulmeister *et al*, 2008; Erbse and Falke, 2009).

The structural information obtained from the chemoreceptor arrays strongly suggests that an Ising-type model with interactions between neighbouring chemoreceptors in an irregular network with variable connectivity is an appropriate mathematical description for receptor cooperativity in bacterial chemotaxis. The observed array structure can be naturally incorporated in the Ising model, from which the response to any given stimulus can be predicted. The agreement between the results from the predicted and the measured responses verifies that the assumptions made in the Ising model are reasonable, and reveals a possible mechanism by which the cell can control the cooperativity

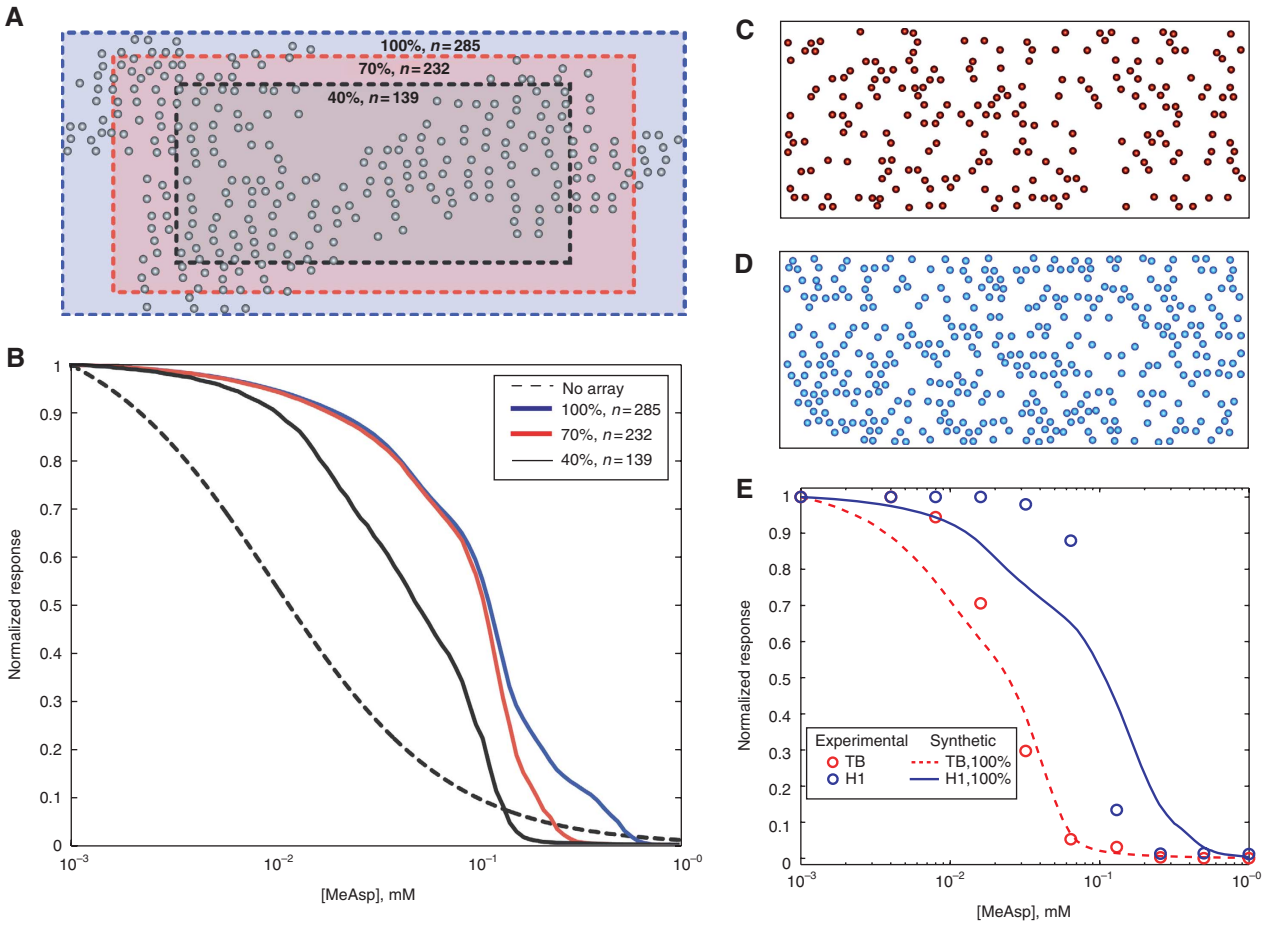

Figure 7 Response curves computed from artificially reduced *E. coli* chemoreceptor sensory arrays and from randomly synthesized lattices. (**A**) Representation of the experimentally determined distribution of signalling complexes within an *E. coli* chemoreceptor array. Rectangles show boxed regions that cover 100, 70, or 40% of the total sensory array area with 285, 232, and 139 nodes, respectively. (**B**) Response curves computed from the reduced *E. coli* chemoreceptor arrays displayed in (**A**) using the proposed Ising-type model: when the array size is large enough to preserve the statistics of connectedness, the artificially reduced array gives rise to very similar response curve as the entire array does (blue and red solid lines); whereas when the array size gets smaller and the statistics of connectedness changes, the response curve of the artificially reduced array (black solid line) deviates from that of the entire chemoreceptor array, and eventually approaches the completely disordered packing arrangement (black dashed line). (**C**, **D**) Randomly synthesized chemoreceptor array distribution plots representing *E. coli* loosely packed chemoreceptor arrays from cells cultured in TB (**C**) and more tightly packed arrays form cells cultured in H1 (**D**). The statistical properties of connectedness in each simulation are controlled to be the same as in corresponding cells. (**E**) Response curves computed from the reduced synthetic distribution plots using the same procedure shown in (**A**). As the lattices are randomly generated, their statistics of connectedness are more homogeneous, which results in relatively small variations in response curves when artificially reducing the size of the lattices (solid and dashed lines).

and sensitivity of its response to stimuli by modulating the 'connectedness' of the chemoreceptor array.

The ability to develop predictive computational models that capture cellular responses to changes in their environment is a central goal of modern cellular biology. Bacterial chemotaxis is among the best-studied signal transduction pathways, and decades of analysis of structural, biochemical, genetic, and physiological components of signalling have contributed to a broad understanding of the overall signalling process. With the advent of advanced imaging methods that allow spatial localization of specific protein complexes within the cell, the prospect of developing an integrated structural understanding of whole bacterial cells at the molecular level is potentially within sight. Chemotaxis is a particularly tractable signalling pathway because of the small number of components involved and the large amount of knowledge about the spatial localization of the receptor end of the signal transduction cascade. The findings we present here show that lateral packing density is a key variable that can be parameterized to develop a predictive, quantitative computational model for chemotaxis. The nature and extent of the bacterial physiological response of the bacterial cells can be predicted to a good approximation using parameters derived from the tomographic data. Clearly, this work only represents a beginning towards development of a more complete quantitative modelling of the overall chemotaxis response, but it provides a platform to refine and explore other physical aspects of receptor packing that could tune the cellular response. The fact that at least some components of whole cells can now be routinely imaged at molecular resolution using cryo-electron tomography (Milne and Subramaniam, 2009), and that the information can be used to develop a testable predictive model is a potentially exciting advance, laying the foundation for further quantitative studies of how the higher order organization of signalling complexes can affect the regulation of function at the cellular level.

Materials and methods

Bacterial strains and culture conditions

E. coli RP437 was grown in either TB media (1.0% tryptone and 0.5% NaCl) or H1 minimal media (1.1% K_2HPO_4/0.48% KH_2PO_4/0.2% $(NH_4)_2SO_4$) with supplements (0.4% glycerol/1 mM of threonine, leucine, methionine, and histidine/1.25 μM FeSO) at 34°C and 280 r.p.m. For FRET experiments, *E. coli* strain VS151 (Δ*tsr* Δ(*cheR cheB cheY cheZ*)) was transformed with plasmid pVS88 that encodes CheY–YFP and CheZ–CFP (Sourjik and Berg, 2004) and expression of fusion proteins was induced by adding 50 μM isopropyl β-D-thiogalactoside (IPTG) to the day culture. For fluorescence imaging experiments, the same strain was transformed with plasmid pVS241 encoding YFP–$CheA_S$, a YFP fusion to the naturally expressed short version of CheA that lacks first 97 amino acids, and expression was induced with 30 μM IPTG.

Specimen preparation, western blot analysis, tomographic data collection, and averaging

Starter cultures were grown overnight at 34°C with 280 r.p.m. shaking to an approximate optical density of 2.0 at 600 nm. Overnight cultures were diluted 1:40 in the same media and grown to a final optical density of 0.5 at 600 nm. Aliquots were immediately mixed with 2 × SDS–PAGE sample buffer and boiled for 5 min. Protein samples were analysed on 10% SDS–PAGE gels that were subsequently transferred to PVDF membranes, blocked, and probed using antisera that react with the highly conserved Tsr signalling domain, CheA, or CheW. For cryo-electron microscopy, bacterial cells (3–5 μl) at an optical density of 0.5 at 600 nm were withdrawn directly from liquid cultures and placed on MultiA Quantifoil grids (Micro Tools GmbH, Germany). The grids were manually blotted or blotted using a Vitrobot robotic freezing device (FEI Corp., OR, USA) and plunge-frozen in liquid ethane maintained at approximately −180°C. For 2D cryo-projection images and cryo-electron tomography, grids containing plunge-frozen cells were placed in cartridges and loaded into the cryo-transfer system of either a Titan Krios or a Polara G2 electron microscope (FEI Corp.). Both microscopes were equipped with a field emission gun operating at 300 kV, and a 2K × 2K CCD camera at the end of a GIF 2000 (Gatan Inc., Pleasanton, CA, USA) energy filtering system. Typically, low-dose tomographic tilt series (0.5–2 e-/Å^2 per image) were collected over an angular range of ± 70° in 1° intervals using a linear tilt scheme at an effective magnification of × 18 000 and underfocus values ranging from 5 to 8 μm. Fiducial-based alignments were performed on full resolution images and three-dimensional reconstructions computed by weighted back projection of aligned images that were binned either 2 × 2 or 4 × 4. Tomographic reconstructions were then processed by 3D non-linear anisotropic diffusion and/or band-pass filtering before segmentation. Alignment, reconstruction, denoising, and segmentation were all preformed using IMOD (Kremer *et al*, 1996) and Amira software packages. To obtain a density map for the distribution of receptors in the plane of the membrane starting from tomograms of whole cells displaying edge-on receptor views, we used three-dimensional alignment procedures similar to those used previously (Khursigara *et al*, 2008a, b). Briefly, ∼1000 sub-volumes of 50 × 50 × 150 in pixels (7.5 Å/pixel) were extracted from the ordered regions of whole cell *E. coli* tomograms to create a stack of sub-volumes. The sub-volumes were classified using a local-maximum clustering method and the major clusters were averaged to create an initial template for further alignment and averaging. The sub-volumes were aligned against the initial template and averaged with hexagonal symmetry imposed in the plane of the receptor array. The averaged image shown in the inset of Figure 1B was derived from averaging 1098 sub-volumes derived from 12 cellular tomograms.

Chemoreceptor array measurements and analysis

Chemoreceptor arrays were segmented from tomographic volumes, and measurements were taken using IMOD (Kremer *et al*, 1996) and Amira software packages. The spatial arrangements of chemosensory molecules were segmented manually, by probing the tomographic volumes one section at a time. A marker was placed at every location where a density corresponding to CheA/W and chemoreceptor would intersect. Immunolabelling experiments have established definitively that these densities correspond to the locations of the CheA/CheW complexes (Zhang *et al*, 2007). Statistical analyses were done using the Prism software package and significant difference between data sets was assessed using a two-sided Mann–Whitney test. Median values were considered significantly different if $P<0.05$.

Nearest neighbour distribution analysis and Ising model

For each array, the pairwise distance (r) between centres of the signalling molecule (CheA/CheW) spots were calculated. The distribution (probability density function) of r, $P(r)$, was then determined. The position (r_{nn}) of the first major peak in $P(r)$ was used to define the average nearest neighbour distance between spots. The nearest neighbours for a given signalling molecule spot in the tomographic volumes were defined as those neighbours within a cutoff distance that could be chosen between the first and the second peak positions of $P(r)$. For our analysis, we chose a cutoff distance of $1.5r_{nn}$, and calculated the average number of nearest neighbours for spots within a given array $\langle nn \rangle_{1.5}$. The value of $\langle nn \rangle_{1.5}$ can be used to characterize the tightness (orderliness) of the array, with higher $\langle nn \rangle_{1.5}$ indicating a tighter array structure. Within the Ising-type model, receptor–receptor interaction is taken into account for neighbouring receptors: a pair of receptors interacts with each other at an interaction energy E_J when their distance is shorter than a cutoff value ($1.5r_{nn}$). The free energy for a given sensory unit in the array can be written as:

$$F(a,m,N_n)=a\times\left(\ln\left(\frac{1+[L]/K_I}{1+[L]/K_A}\right)+E_M(m)+\sum_{i=1}^{N_n}E_J\cdot\left(\frac{1}{2}-a_i\right)+E_G(N_n)\right),$$

where $a=0$, 1 represent the active and inactive states of the receptor and N_n is the number of nearest neighbours. The strength of the nearest neighbour interaction energy can be estimated to be a few k_BT (the thermal energy) from previous dose–response data and the corresponding modelling studies (4, 5). Here, we used $E_J=2.75\,k_BT$, which results in a good agreement with the experiments. $[L]$ is the ligand concentration and the first term in the energy expression comes from ligand binding. The dissociation constants K_I, K_A for the inactive and active chemoreceptors were determined based on previous work (Sourjik and Berg, 2002b, 2004; Mello and Tu, 2007). The methylation level of the receptor is represented by m and $E_M(m)$ is the methylation level-dependent energy term $E_M(m)=E_M(0)-e_m m$ with $e_m\approx 2k_BT$ (Shimizu *et al*, 2010). Finally, E_G represents the energy contribution from the non-receptor components in the complex. The detailed form of E_G is unknown. In this work, we lumped energy contributions from all non-sensor components within the interaction range of a sensor by E_0 for simplicity. As E_0 is shared by $(1+N_n)$ receptors within the defined nearest neighbourhood, the contribution to each receptor is on average $E_G=E_0/(1+N_n)$. There are other possible forms of E_G that are also in agreement with the available data. For a given chemoreceptor array topology from tomographic experiments, the Ising model was solved by Monte–Carlo simulations. The sensory adaptation in the wild-type cells is carried out by the receptor methylation process, which we modelled here by adopting the same approach as used by Mello and Tu (2003), where the methyltransferase CheR and the methylesterase CheB-P act on inactive and active receptors, respectively, to achieve (near) perfect adaptation. The methylation $k_R=1$ is used to set the time scale, and $k_B=2$ is used so that the adapted activity is 1/3 (Figure 3). In the *cheRB* mutants, receptor modification ($m=2$) is fixed and the cells do not adapt, but they do respond in a narrow range of ligand concentrations, which depend on N_n through the global energy term as shown in Figure 6, where $E_0=25\,k_BT$, $E_M(0)=-4.5\,k_BT$ gives excellent agreement between theory and experiment for cells cultured in either TB or H1 media.

For the experiments that determined the effects of varying size versus packing density of the chemoreceptor array, three rectangles were chosen to cover either the whole array (100%) or sub-regions of the array (70 or 40%). The synthetic lattices used were generated by random deletion of different fractions of nodes in a two-dimensional honeycomb lattice, and the remaining nodes were randomly shuffled within a certain radius to generate a random distribution. The packing of the synthetic lattices was chosen to reflect

the same nearest neighbour statistics observed experimentally for growth in H1 and TB media. The loosely packed lattice has a fractional occupancy of ~30%, while the tightly packed lattice has a fractional occupancy of ~50%. Each dose–response curve is the result of averaging 100 000 independent simulations.

FRET and imaging analyses

Cell preparation and FRET measurements were performed as described previously (Sourjik *et al*, 2007; Neumann *et al*, 2010). Cells were grown to $OD_{600} = 0.45$, washed twice with tethering buffer (10 mM potassium phosphate, 0.1 mM EDTA, 1 mM L-methionine, 10 mM sodium lactate, pH 7.0) by centrifugation at 4000 r.p.m., left for at least 30 min at 4°C, concentrated about 100-fold by centrifugation, attached to a polylysine-coated coverslip and placed into a flow chamber, mounted on a custom-modified Zeiss Axio Imager Z.1 microscope equipped with a ×40/0.75 EC Plan-Neofluar objective and controlled by Axiovision software. The chamber was maintained at 20°C and under a constant flow (0.5 ml/min) of tethering buffer by a syringe pump (Harvard Apparatus). The same flow was used to add and remove specified amounts of attractant α-methyl-D,L-aspartate (MeAsp; Sigma) in tethering buffer in a sequence of steps of increasing concentration. CFP fluorescence of a dense monolayer was excited at 436/20 nm through a 455-nm dichroic mirror by a 75-W Xenon lamp attenuated 500-fold with neutral density filters. CFP and YFP emissions were detected through 480/40 nm band pass and 520 nm long-pass emission filters, respectively, and signals from 300 to 500 cells were collected with an integration time of 1 s by Peltier-cooled photon counters (Hamamatsu) equipped with a PCI-6034 counting board connected to a computer with custom written LabView7 software (both from National Instruments). FRET was defined as a fractional change in CFP fluorescence due to energy transfer, and calculated from changes in the ratios of yellow and cyan fluorescence signals upon stimulation as described before (Sourjik *et al*, 2007). The same microscope equipped with an ORCA AG CCD camera (Hamamatsu) was used for imaging of cells that were immobilized on an agarose pad.

Acknowledgements

This work was supported by funds from the Center for Cancer Research, National Cancer Institute, NIH (to SS) and from the Deutsche Forschungsgemeinschaft (grant SO 421/7-1 to SN and VS). We thank Dr Martin Kessel for useful discussions during the course of this work.

Conflict of interest

The authors declare that they have no conflict of interest.

References

Borgnia MJ, Subramaniam S, Milne JL (2008) Three-dimensional imaging of the highly bent architecture of Bdellovibrio bacteriovorus by using cryo-electron tomography. *J Bacteriol* **190:** 2588–2596

Bornhorst JA, Falke JJ (2003) Quantitative analysis of aspartate receptor signaling complex reveals that the homogeneous two-state model is inadequate: development of a heterogeneous two-state model. *J Mol Biol* **326:** 1597–1614

Bray D, Levin MD, Morton-Firth CJ (1998) Receptor clustering as a cellular mechanism to control sensitivity. *Nature* **393:** 85–88

Briegel A, Ding HJ, Li Z, Werner J, Gitai Z, Dias DP, Jensen RB, Jensen GJ (2008) Location and architecture of the Caulobacter crescentus chemoreceptor array. *Mol Microbiol* **69:** 30–41

Briegel A, Ortega DR, Tocheva EI, Wuichet K, Li Z, Chen S, Muller A, Iancu CV, Murphy GE, Dobro MJ, Zhulin IB, Jensen GJ (2009) Universal architecture of bacterial chemoreceptor arrays. *Proc Natl Acad Sci USA* **106:** 17181–17186

Duke TA, Bray D (1999) Heightened sensitivity of a lattice of membrane receptors. *Proc Natl Acad Sci USA* **96:** 10104–10108

Erbse AH, Falke JJ (2009) The core signaling proteins of bacterial chemotaxis assemble to form an ultrastable complex. *Biochemistry* **48:** 6975–6987

Gegner JA, Graham DR, Roth AF, Dahlquist FW (1992) Assembly of an MCP receptor, CheW, and kinase CheA complex in the bacterial chemotaxis signal transduction pathway. *Cell* **70:** 975–982

Hansen CH, Sourjik V, Wingreen NS (2010) A dynamic-signaling-team model for chemotaxis receptors in Escherichia coli. *Proc Natl Acad Sci USA* **107:** 17170–17175

Hazelbauer GL, Falke JJ, Parkinson JS (2008) Bacterial chemoreceptors: high-performance signaling in networked arrays. *Trends Biochem Sci* **33:** 9–19

Kentner D, Sourjik V (2006) Spatial organization of the bacterial chemotaxis system. *Curr Opin Microbiol* **9:** 619–624

Keymer JE, Endres RG, Skoge M, Meir Y, Wingreen NS (2006) Chemosensing in Escherichia coli: two regimes of two-state receptors. *Proc Natl Acad Sci USA* **103:** 1786–1791

Khursigara CM, Wu X, Subramaniam S (2008a) Chemoreceptors in Caulobacter crescentus: trimers of receptor dimers in a partially ordered hexagonally packed array. *J Bacteriol* **190:** 6805–6810

Khursigara CM, Wu X, Zhang P, Lefman J, Subramaniam S (2008b) Role of HAMP domains in chemotaxis signaling by bacterial chemoreceptors. *Proc Natl Acad Sci USA* **105:** 16555–16560

Kremer JR, Mastronarde DN, McIntosh JR (1996) Computer visualization of three-dimensional image data using IMOD. *J Struct Biol* **116:** 71–76

Li G, Weis RM (2000) Covalent modification regulates ligand binding to receptor complexes in the chemosensory system of Escherichia coli. *Cell* **100:** 357–365

Li M, Hazelbauer GL (2004) Cellular stoichiometry of the components of the chemotaxis signaling complex. *J Bacteriol* **186:** 3687–3694

Maddock JR, Shapiro L (1993) Polar location of the chemoreceptor complex in the Escherichia coli cell. *Science* **259:** 1717–1723

Mello BA, Tu Y (2003) Quantitative modeling of sensitivity in bacterial chemotaxis: the role of coupling among different chemoreceptor species. *Proc Natl Acad Sci USA* **100:** 8223–8228

Mello BA, Tu Y (2005) An allosteric model for heterogeneous receptor complexes: understanding bacterial chemotaxis responses to multiple stimuli. *Proc Natl Acad Sci USA* **102:** 17354–17359

Mello BA, Tu Y (2007) Effects of adaptation in maintaining high sensitivity over a wide range of backgrounds for Escherichia coli chemotaxis. *Biophys J* **92:** 2329–2337

Milne JL, Subramaniam S (2009) Cryo-electron tomography of bacteria: progress, challenges and future prospects. *Nat Rev Microbiol* **7:** 666–675

Neumann S, Hansen CH, Wingreen NS, Sourjik V (2010) Differences in signaling by directly and indirectly binding ligands in bacterial chemotaxis. *EMBO J* **29:** 3484–3495

Schulmeister S, Ruttorf M, Thiem S, Kentner D, Lebiedz D, Sourjik V (2008) Protein exchange dynamics at chemoreceptor clusters in Escherichia coli. *Proc Natl Acad Sci USA* **105:** 6403–6408

Segall JE, Block SM, Berg HC (1986) Temporal comparisons in bacterial chemotaxis. *Proc Natl Acad Sci USA* **83:** 8987–8991

Shimizu TS, Aksenov SV, Bray D (2003) A spatially extended stochastic model of the bacterial chemotaxis signaling pathway. *J Mol Biol* **329:** 291–309

Shimizu TS, Tu Y, Berg HC (2010) A modular gradient-sensing network for chemotaxis in Escherichia coli revealed by responses to time-varying stimuli. *Mol Syst Biol* **6:** 382

Sourjik V, Armitage JP (2010) Spatial organization in bacterial chemotaxis. *EMBO J* **29:** 2724–2733

Sourjik V, Berg HC (2000) Localization of components of the chemotaxis machinery of Escherichia coli using fluorescent protein fusions. *Mol Microbiol* **37:** 740–751

Sourjik V, Berg HC (2002a) Binding of the Escherichia coli response regulator CheY to its target measured *in vivo* by fluorescence resonance energy transfer. *Proc Natl Acad Sci USA* **99:** 12669–12674

Sourjik V, Berg HC (2002b) Receptor sensitivity in bacterial chemotaxis. *Proc Natl Acad Sci USA* **99:** 123–127

Sourjik V, Berg HC (2004) Functional interactions between receptors in bacterial chemotaxis. *Nature* **428:** 437–441

Sourjik V, Vaknin A, Shimizu TS, Berg HC (2007) *In vivo* measurement by FRET of pathway activity in bacterial chemotaxis. *Methods Enzymol* **423:** 365–391

Thiem S, Kentner D, Sourjik V (2007) Positioning of chemosensory clusters in E. coli and its relation to cell division. *EMBO J* **26:** 1615–1623

Wadhams GH, Armitage JP (2004) Making sense of it all: bacterial chemotaxis. *Nat Rev Mol Cell Biol* **5:** 1024–1037

Zhang P, Khursigara CM, Hartnell LM, Subramaniam S (2007) Direct visualization of Escherichia coli chemotaxis receptor arrays using cryo-electron microscopy. *Proc Natl Acad Sci USA* **104:** 3777–3781